ACS Photonics

Article

Cite This: ACS Photonics 2019, 6, 351−359

pubs.acs.org/journal/apchd5

# Flexible X-ray Detectors Based on Amorphous $Ga_2O_3$ Thin Films

Huili Liang,*[,†] Shujuan Cui,[†,‡] Rui Su,[§] Pengfei Guan,[§,∥] Yuhang He,[⊥] Lihong Yang,[#] Liming Chen,[⊥] Yonghui Zhang,[†,‡] Zengxia Mei,*[,†] and Xiaolong Du[†,‡]

[†]Key Laboratory for Renewable Energy, Beijing National Laboratory for Condensed Matter Physics, Institute of Physics (IOP), Chinese Academy of Sciences, Beijing 100190, China

[‡]School of Physical Sciences, University of Chinese Academy of Sciences, Beijing 100049, China

[§]Innovative Center for Advanced Materials (ICAM), Hangzhou Dianzi University, Hangzhou 310012, China

[∥]Beijing Computational Science Research Center, Beijing 100193, China

[⊥]Key Laboratory for Optical Physics, Beijing National Laboratory for Condensed Matter Physics, Institute of Physics (IOP), Chinese Academy of Sciences, Beijing 100190, China

[#]National Laboratory for Superconductivity, Beijing National Laboratory for Condensed Matter Physics, Institute of Physics (IOP), Chinese Academy of Sciences, Beijing 100190, China

Supporting Information

**ABSTRACT:** $Ga_2O_3$, as an emerging optoelectronic material, is very appealing for the detection of ionizing radiation because of its low cost, wide band gap (4.5−5.0 eV) and radiation hardness. In this work, a flexible X-ray detector using amorphous $Ga_2O_3$ (*a*-$Ga_2O_3$) thin film is demonstrated. The *a*-$Ga_2O_3$ thin film was deposited on polyethylene naphthalate (PEN) substrate with delicately control of the oxygen flux during the radio frequency (RF) magnetron sputtering process. Metal/semiconductor/metal-structured photodetectors with coplanar interdigital electrodes were fabricated on this *a*-$Ga_2O_3$ film. Temporal response measurements under X-ray illumination indicate that a larger photocurrent occurs on the film deposited with smaller oxygen flux. A model combined with theoretical calculation is proposed to explain the enhancement of the X-ray photoresponsivity, which involves the slowing down of the annihilation rate caused by the neutralization of more ionized oxygen vacancy ($V_o$) states. No significant degradation of the device performance under UV and X-ray radiation is observed after the flexibility test. This finding informs a novel way to design the flexible X-ray and other ionizing radiation detectors based on amorphous oxide materials.

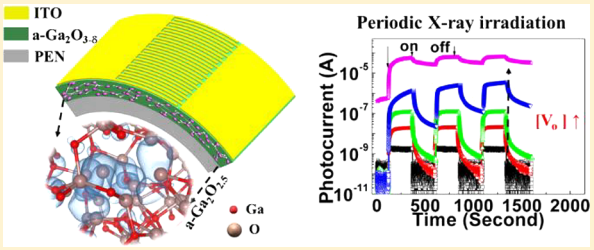


**KEYWORDS:** *amorphous $Ga_2O_3$, flexible, X-ray detectors, oxygen vacancy, persistent photocurrent*

X-rays are part of the electromagnetic spectrum, with wavelengths shorter than the ultraviolet range. The detection of X-rays is important for broad applications such as medical imaging, cancer treatment, industrial nondestructive testing, public security inspection, X-ray space communication, and so on. Nowadays wearable electronics and printable electronics are developing so quickly that the demand for large-area, flexible, and lightweight radiation detectors is also increasing. This new type detector is not only very portable and cost-effective, but also can be readily shaped to fit the nonplanar surfaces such as cracked oil pipelines or body injury sites. Therefore, great efforts have been devoted to fabricating such flexible X-ray detectors.[1−5] At the initial stage, the flexibility characteristic was realized through reducing the whole thickness of the device, where the combination of a conventional amorphous Si (*a*-Si) PIN photodiode and scintillator was developed.[1] In this case, a big challenge is to find the balance between film stress and film quality, as reported in ref 1. Organic photodetectors (OPDs) are another candidate for flexible X-ray detectors due to their easier fabrication process and superior mechanical behavior.[2,3] All-printed flexible X-ray detectors using inkjet-printed OPDs combined with water-based and stretchable scintillator ink have been developed by J. Oliveira et al. recently.[4−6] It is an increasingly proposed technique for the fabrication of flexible X-ray detectors. Several other flexible X-ray detectors have also been reported using sliced $PbI_2$ or organic thin films.[7,8] However, the obstacles for the commercializing of the above-mentioned detectors are how to fabricate a uniform and homogeneous layer over a large area and how to maintain their stability and repeatability under long X-ray irradiations.

Meanwhile, new materials have been increasingly exploited to be applied in X-ray detection. Organic single crystals,[9] hybrid organic−inorganic perovskites (HOIPs),[10−15] semiconducting polymer blended with high-*Z* absorbers,[16] GaN,[17]

Received: June 7, 2018
Published: December 26, 2018






DOI: 10.1021/acsphotonics.8b00769
ACS Photonics 2019, 6, 351−359

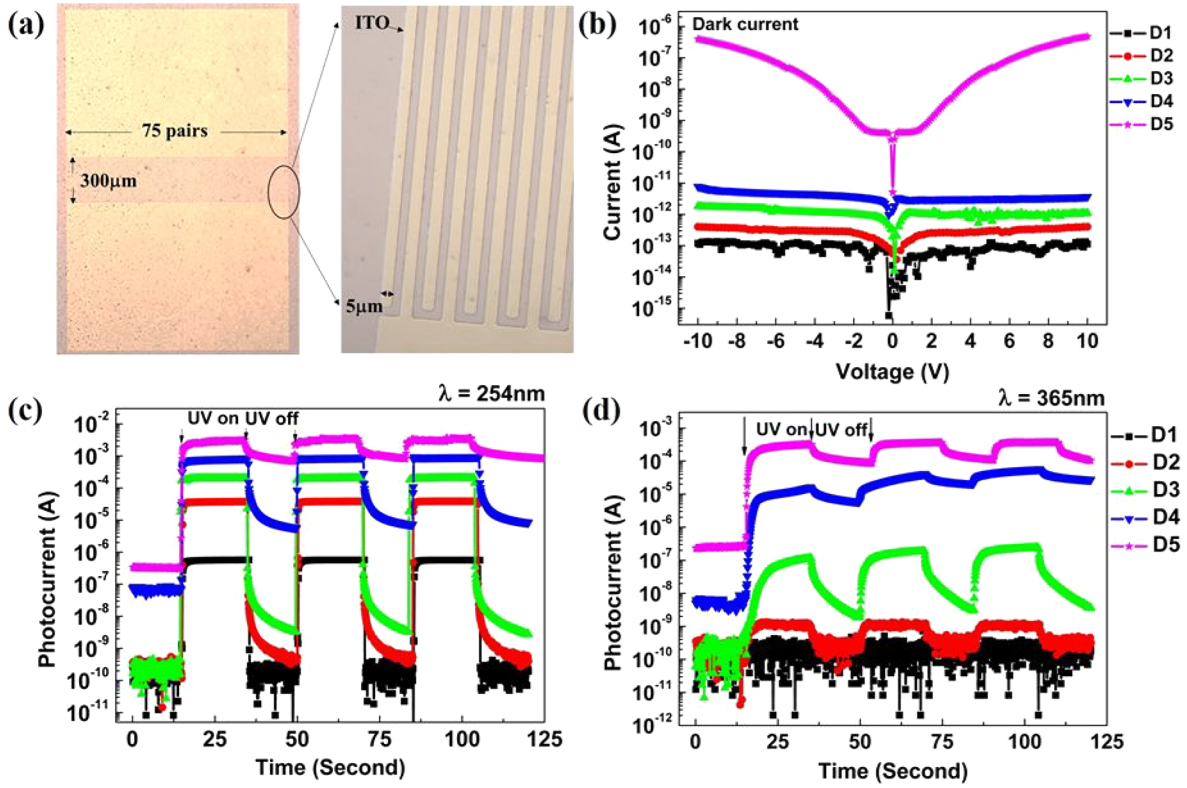


**Figure 1.** (a) Microscope photograph of the MSM-structured *a*-$Ga_2O_3$ X-ray detector on PEN substrate. (b) *I*−*V* curves under darkness. (c) Time-dependent photocurrent of D1−D5 with the UV 254 nm light on and off at 10 V bias. (d) Time-dependent photocurrent of D1−D5 with the UV 365 nm light on and off at 10 V bias.

and diamond[18] have emerged as next-generation direct X-ray detectors. Even though the performance of the HOIP detectors is shining, special care should be taken on the issue of device degradation due to the X-ray-irradiation-induced structural and/or compositional changes.[19] Moreover, all of these detectors are envisaged on single-crystal or polycrystalline active layers and cannot satisfy the requirement of the mechanical flexibility. Wide-band-gap oxide semiconductors (e.g., ZnO, In−Ga−Zn−O, amorphous $Ga_2O_3$), on the other hand, possessing the merits of natural excellent radiation hardness and easy fabrication at low temperatures, have been developed to fabricate different flexible devices such as thin film transistors (TFTs),[20] field-effect diodes,[21] and photodetectors.[22] However, to the best of our knowledge, flexible X-ray detectors using the aforementioned oxides have not been reported yet, although many groups have claimed that ZnO can be potentially designed to be a rigid X-ray detector.[23,24]

Amorphous $Ga_2O_3$ (*a*-$Ga_2O_3$), with the advantage of low growth temperature, has exhibited excellent optoelectronic performance,[22,25] indicating it may potentially work as a promising flexible X-ray photoconverter. In this work, we report for the first time a flexible X-ray detector based on *a*-$Ga_2O_3$ thin film, which is deposited on polyethylene naphthalate (PEN) substrate at room temperature (RT) by a radio frequency (RF) magnetron sputtering system with subtle control of the oxygen flux. Metal/semiconductor/metal-structured (MSM-structured) photodetectors with coplanar interdigital electrodes are fabricated to serve as X-ray sensors. Temporal response measurements indicate that when the oxygen gas is less adopted, the X-ray photocurrent would be larger. For an understanding of this phenomenon, photoresponse characteristics of the devices are investigated under illumination of various wavelengths, and a schematic diagram of the sub-band-gap states is deduced, which is coincident with theoretical results using density functional theory (DFT) calculation. According to these results, the enhancement of the current induced by X-rays is tentatively interpreted as a consequence of the slowing down of the annihilation rate caused by the neutralization of more ionized oxygen vacancy ($V_o$) states. Flexibility tests show no obvious degradation of the device performance under UV and X-ray irradiation, demonstrating the robustness of the flexible X-ray detectors.

## RESULTS AND DISCUSSION

As mentioned above, oxygen flux was delicately controlled during the sputtering process, which was realized through the combination of a gas leakage valve and *in situ* ion-gauge monitoring. Five samples with different oxygen partial pressures ($1.6 \times 10^{-3}$, $1.4 \times 10^{-3}$, $1.2 \times 10^{-3}$, $1.0 \times 10^{-3}$, and 0 Pa) were prepared and labeled as D1, D2, D3, D4, and D5, respectively. (For more details about the film characteristics, please see ref 22.) MSM-structured photodetectors with coplanar interdigital electrodes were fabricated as shown in Figure 1a. Figure 1b presents *I*−*V* curves of the five $Ga_2O_3$ prototype devices in darkness. The dark current at a bias of 10 V is kept at a picoampere level in all devices except D5 (0.4 μA), which ensures high signal/noise (S/N) ratios. It is quite obvious that the dark current increases gradually as the oxygen partial pressure decreases, which is related to the lowered Schottky barrier height (SBH) at the interface of ITO/*a*-$Ga_2O_3$ as illustrated in our previous work.[22] Figure 1c gives time-dependent responses of all samples under 254 nm ultraviolet (UV) light at 10 V bias. All devices demonstrate


DOI: 10.1021/acsphotonics.8b00769
ACS Photonics 2019, 6, 351−359

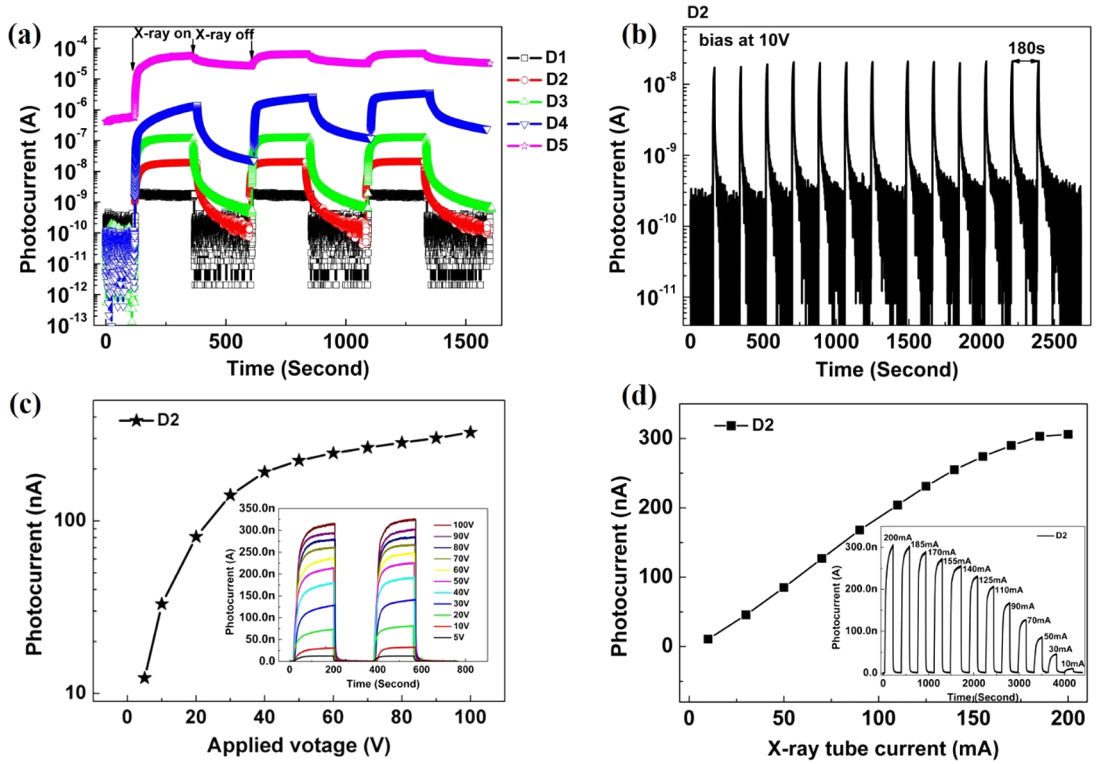


**Figure 2.** (a) Time-dependent photocurrent of D1−D5 with X-ray source on and off at 10 V bias. (b) Time-dependent photocurrent of D2 with pulsed X-ray source on and off at 10 V bias. (c) Photocurrent of D2 as a function of the applied bias. The photocurrent value is taken from the 2nd cycle before the X-ray is off. (d) Photocurrent as a function of the incident X-ray tube current. The photocurrent value is taken before the X-ray is off, and the applied voltage is $V$ = 100 V.

good repeatability of response to the periodical UV light illumination. It is worth noting that the photocurrent increases about 4 orders of magnitude as oxygen partial pressure decreases, which should benefit from the decrease of the SBHs, in agreement with the trend of the dark current. Additionally, the persistent photocurrent (PPC) effect becomes more and more remarkable as oxygen flux decreases, which is believed to be related to $V_o$ and also helpful for the increase of photocurrents.[26,27] For a further investigation of the behavior of $V_o$ defects, all samples were illuminated by 365 nm UV light, which is beneath the band gap of $a$-$Ga_2O_3$ (∼5.03 eV)[22] and cannot excite band to band transition. The corresponding photocurrents were recorded as shown in Figure 1d. It can be found that photoresponse from UV 365 nm decreases greatly from D5 to D1, indicating an evident dependence on the concentration of $V_o$. Electrons excited from sub-band-gap localized states make an obvious contribution to the measured photocurrent. From the above $I$−$V$ curves and the temporal responses under UV light, it can be seen that all devices behave as decent UV detectors, which is consistent with our previous report.[22]

The important point here is how these devices behave under X-ray irradiation. Therefore, we measured their responses to X-ray illumination. The source is an X-ray tube working at 40 kV with a Cu anode, equipped in an X-ray diffraction setup. Figure 2a is the transient response with X-rays on and off (controlled by an electromechanical shutter) for 3 cycles at 10 V bias. Similar to the UV response shown in Figure 1c,d, all devices demonstrate good repeatability. Importantly, photocurrents also increase 4 orders of magnitude as $V_o$ concentration increases from D1 to D5. Note that both the rise and decay times of D1 are quite fast and without obvious PPC effect, which is distinctly different from other devices. This fast transient rise feature is also observed right after the initial illumination on D2, D3, and D4 in a level of 1∼2 nA (which can be clearly distinguished from the subsequent slow rise in Figure S1, Supporting Information), but merging into the dark current of D5 and difficult to recognize. This quick photocurrent has been reported in GaN X-ray detectors and is considered to increase linearly with incident X-ray power.[17] T. Cramer et al. investigated the radiation tolerance of oxide TFT to X-ray exposure and found that both the off current and leakage current were increased from picoampere to nanoampere levels, which was attributed to the air ionization effect.[28] This viewpoint can be further consolidated by the work of D. Brivio et al., where they used high-energy current to detect X-ray signals.[29] Interestingly, a subsequent long turn-on transient appears in D2, D3, D4, and D5, which has also been observed in GaN and diamond X-ray detectors.[17,30] They just ascribed this behavior to defect traps and did not provide any strategy to control these traps. In our work, it can be clearly seen that such a trap is related to oxygen and can be delicately controlled. Further, D2 was exposed to the X-ray source with a pulse width of 10 s, and Figure 2b is the current variation for 13 cycles at 10 V bias. From this figure, it can be seen that the dark current decreases quickly, implying a potential application in X-ray detection. However, this quick decay time is realized at the price of the decreased photocurrent. In the future, a gated three-terminal device architecture[31] will be considered to speed up the decay rate and hold a large photocurrent at the same time. Figure 2c reports the variation of the X-ray photocurrent with different bias voltages. The X-ray-induced



DOI: 10.1021/acsphotonics.8b00769
ACS Photonics 2019, 6, 351−359

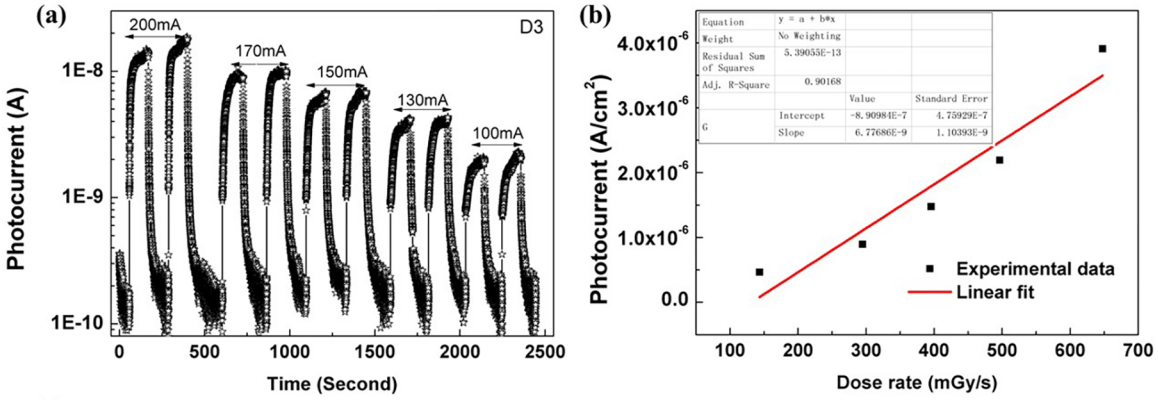


(c)

| Material | Thickness (μm) | Voltage (V) | Sensitivity in the reference | Normalized sensitivity by active volume ($\mu C\ mGy_{air}^{-1}\ cm^{-3}$) |
|---|---|---|---|---|
| Pentacene Ref. 8 | 0.1 | 0.2 | 77,000 nC $mGy^{-1}\ cm^{-3}$ | 77 |
| $CH_3NH_3PbI_3$ Ref. 10 | 0.6 | 0 | 25 $\mu C\ mGy_{air}^{-1}\ cm^{-3}$ | 25 |
| $MAPbBr_3$ Ref. 11 | 2000 | -0.1 | 80 $\mu C\ Gy_{air}^{-1}\ cm^{-2}$ | 0.4 |
| $MAPbBr_3$ Ref. 12 | 150 | -7 | $2.1 \times 10^4\ \mu C\ Gy_{air}^{-1}\ cm^{-2}$ | 1400 |
| $MAPbI_3$ Ref. 13 | 1000 | 200 | 2527 $\mu C\ Gy_{air}^{-1}\ cm^{-2}$ | 25.27 |
| ZnO Ref. 23 | 500 | 50 | 19.4 nC $Gy^{-1}$ | $6.1 \times 10^{-4}$ |
| ZnO Ref. 24 | 500 | 20 | 1.5 μC $Gy^{-1}$ | 5.68 |
| a-Se Ref. 33 | 200 | 2000 | 220 pC $cm^{-2}\ mR^{-1}$ | 1.25 |
| a-$Ga_2O_3$ this work | 0.25 | 50 | 271 $\mu C\ mGy_{air}^{-1}\ cm^{-3}$ | 271 |

**Figure 3.** (a) Time-dependent photocurrent of D3 with a 120 s long X-ray illumination at 50 V bias. (b) X-ray-generated photocurrent at various dose rates. The photocurrent value is taken from the 2nd cycle before the X-ray is off. A sensitivity of $6.77 \times 10^{-3}$ $\mu C\ mGy_{air}^{-1}\ cm^{-2}$ is derived from the slope of the fitting line. (c) Comparison with the sensitivity of the various detectors presented in the reference. All of the sensitivity values have been normalized with the active volume.

current increases quickly at first (lower than 40 V) and then tends to saturate gradually, meaning that nearly all the photo-created electron−hole (e−h) pairs have been collected by the electrodes. Moreover, it should be noted that the applied voltage has not reached the avalanche breakdown value, and thus, the carrier multiplication phenomenon[32] should be excluded as the source of photoconductive gain. Figure 2d shows the X-ray photocurrents of D2 as a function of the incident X-ray power biased at 100 V. It can be observed that the saturated photocurrent increases almost linearly with the X-ray tube current. It is noteworthy that we spent about 5 h to complete the above measurement. That is, the device was biased at 100 V persistently and exposed to X-ray radiation periodically, indicating a superior stability of our device under high voltage and hard radiation.

In Figure 3a, we measured the X-ray photocurrents of D3 illuminated with different dose rates calculated in the Supporting Information. It should be noted that the bias was increased to 50 V from the original 10 V, because the intensity of the X-ray beam decreased a lot after monochromatization. From the linear fit of the experimental data (Figure 3b), the slope of the line, i.e., the device sensitivity, was determined as $6.77 \times 10^{-3}$ $\mu C\ mGy_{air}^{-1}\ cm^{-2}$. Note that the active layer is very thin (~250 nm) in our case. If we take the layer thickness into account, as what was done in ref 10, the sensitivity value can be 271 $\mu C\ mGy_{air}^{-1}\ cm^{-3}$, much higher than the commercial *a*-Se X-ray detector (reported in the range 1−17 $\mu C\ mGy_{air}^{-1}\ cm^{-3}$ depending on the operating field and thickness[33]). We further compared the sensitivity value of our device with various detectors presented in the listed references as shown in Figure 3c. All of the sensitivity values have been normalized with the active volume. The result clearly indicates that amorphous $Ga_2O_3$ has great potential in direct detection of X-ray radiation.

To explore the enhancement mechanism of the X-ray photocurrent, we compared the transient characteristics of the photocurrents induced by UV 254 nm (shown in Figure 1c) and X-ray radiation (shown in Figure 2a). As reported before, stretched exponential fits have been successfully employed to characterize many amorphous materials like *a*-Si,[34] *a*-IGZO,[27,35] and so on. Here, we also use the stretched exponential function, as shown in the following, to simulate the transient behavior of the photocurrents under UV light and X-rays.



DOI: 10.1021/acsphotonics.8b00769
ACS Photonics 2019, 6, 351−359

**Table 1. Stretched Exponential Fitting Results of the Photo-excitation and Dark Relaxation Data for the Second Cycle of All Samples under UV Light or X-ray Irradiation[a]**

| | | photoexcitation | | | | dark relaxation | | | |
|---|---|---|---|---|---|---|---|---|---|
| device | illumination source | $\tau$ (s) | $\beta$ | $I_s$ (A) | $I_0$ (A) | $\tau$ (s) | $\beta$ | $I_s$ (A) | $I_0$ (A) |
| D1 | UV 254 | 0.54 | 0.80 | $5.62 \times 10^{-7}$ | $-6.07 \times 10^{-7}$ | | | | |
| D2 | UV 254 | 0.62 | 0.65 | $3.90 \times 10^{-5}$ | $-4.34 \times 10^{-5}$ | 0.06 | 0.44 | $7.82 \times 10^{-10}$ | $1.51 \times 10^{-7}$ |
| | X-ray | 15.5 | 0.80 | $2.03 \times 10^{-8}$ | $-1.99 \times 10^{-8}$ | 1.1 | 0.34 | $1.12 \times 10^{-10}$ | $1.97 \times 10^{-8}$ |
| D3 | UV 254 | 0.64 | 0.58 | $1.88 \times 10^{-4}$ | $-2.10 \times 10^{-4}$ | 0.30 | 0.50 | $4.04 \times 10^{-9}$ | $3.16 \times 10^{-7}$ |
| | X-ray | 22.5 | 0.65 | $1.15 \times 10^{-7}$ | $-1.27 \times 10^{-7}$ | 1.8 | 0.42 | $7.67 \times 10^{-10}$ | $8.97 \times 10^{-8}$ |
| D4 | UV 254 | 0.67 | 0.65 | $8.21 \times 10^{-4}$ | $-9.25 \times 10^{-4}$ | 0.32 | 0.51 | $6.71 \times 10^{-6}$ | $1.42 \times 10^{-4}$ |
| | X-ray | 50.1 | 0.67 | $2.65 \times 10^{-6}$ | $-2.52 \times 10^{-6}$ | 3.3 | 0.45 | $2.72 \times 10^{-8}$ | $1.36 \times 10^{-6}$ |
| D5 | UV 254 | 1.20 | 0.56 | $2.92 \times 10^{-3}$ | $-3.34 \times 10^{-3}$ | 5.01 | 0.64 | $5.38 \times 10^{-4}$ | $1.03 \times 10^{-3}$ |
| | X-ray | 68.3 | 0.74 | $6.10 \times 10^{-5}$ | $-6.26 \times 10^{-5}$ | 51.3 | 0.45 | $2.13 \times 10^{-5}$ | $3.64 \times 10^{-5}$ |

[a]The $\tau$, $\beta$, $I_s$, and $I_0$ values are deduced from best fits to the data.

$$I(t) = I_s + I_0 \exp\left[-\left(\frac{t}{\tau}\right)^{\beta}\right]$$

Here, $I(t)$ is time-dependent current; $I_s$ is either the saturation photocurrent under illumination, or the final relaxed dark current depending on experimental conditions; $I_0$ is a prefactor; $\tau$ is the effective time constant; and $\beta$ is the stretching exponent. $\tau$ can be defined as the time when the time-dependent current $I(t)$ relaxes to $1/e$ of its initial value $I_0$ under darkness. The stretched exponential fitting curves can be found in Figure S2, Supporting Information. Table 1 lists all of the fitting parameters, from which we can clearly find that the time constants, for both photo-excitation and dark relaxation conditions, are increasing as the oxygen partial pressure decreases from D1 to D5 no matter what the illumination source is. Besides that, $I_s$ values, under both UV and X-ray excitation, are also boosted from D1 to D5. In addition, for dark relaxation, it has been reported the ratio $I_s/I_0$ is so small that accurate fits can be achieved under the approximation $I_s = 0$.[35] However, in our case, the ratio $I_s/I_0$ becomes larger and larger, from about 5‰ in D1 to above 50% in D5, indicating that extrinsic doping is introduced and comparable with the photoinduced carrier density.[35] According to the comparison between UV and X-ray responses, it is suspected that there is something in common between UV and X-ray excitations.

Further, three representative samples (D1, D2, and D5) were illuminated with various wavelengths between 200 and 700 nm. To eliminate the influence of the PPC effect, the photocurrent data acquisition was performed by illuminating the devices from long wavelength to short wavelength manually. Figure 4a shows the corresponding results. A red-shift of the cutoff-wavelength is distinctly observed in D1, D2, and D5, which is consistent with our previous report.[22] Moreover, even visible light can create e−h pairs, making a contribution to the photocurrent as shown in sample D5. The photoresponse of visible light is apparently at variance with the optical transparency of *a*-$Ga_2O_3$, which has also been observed in *a*-IGZO.[36] This phenomenon is attributed to an intrinsic nature of amorphous materials caused by tail states from the valence band[36] due to the lack of long-range order.[37] J. T. Jang et al. reported sputtering deposition of *a*-IGZO and found that smaller oxygen flow rates would result in more pronounced PPC, and larger densities of valence band tail (VBT) states.[38] In our samples, as long as the excitation wavelength is shorter than the cutoff value, a photoresponse will happen, confirming the existence of the continuous VBT states. On the basis of these facts, a schematic diagram of the sub-band-gap states is deduced as shown in Figure 4b. Large densities of VBT states are expanded into the band gap as more and more oxygen vacancies are produced with small oxygen flux. Therefore, the onset of the photoresponse exhibits a red-shift from about 320 nm (~3.9 eV) in D1 to about 600 nm (~2.0 eV) in D5. Electrons from VBT states contribute a lot to the photocurrents. Meanwhile, the $V_o$ defects can also be ionized to $V_o^{2+}$ states by the photoexcitation, donating two electrons to the conduction band,[39] which is another source of the photoinduced carriers.

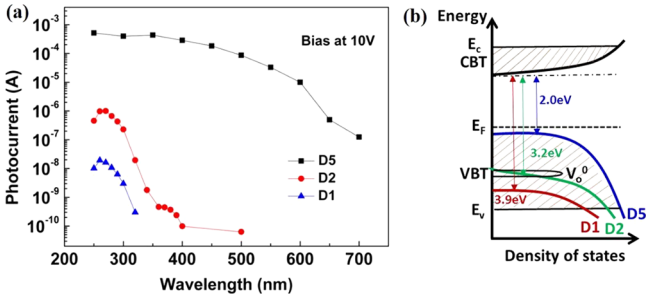


**Figure 4.** (a) Photocurrents of D1, D2, and D5 under illumination with various wavelengths biased at 10 V. (b) Schematic diagram of the sub-band-gap states for D1, D2, and D5.

For a further survey of the sub-band-gap states in *a*-$Ga_2O_3$ thin films with different $V_o$ concentration, DFT calculations are performed by using the Vienna *ab initio* simulation package (VASP).[40] The valence−core interaction is described by the projected augmented wave method. The PBE functional is used to describe the exchange correlation effect.[41] As the PBE functional underestimates the band gap of $Ga_2O_3$, the HSE06 functional[42] is used to calculate the electron structure of amorphous structures. Figure 5a−c shows the calculated electron structure of neutral ($Ga_{48}O_{72}$) and oxygen-deficient ($Ga_{48}O_{68}$, $Ga_{48}O_{60}$) *a*-$Ga_2O_3$. The localization of the electron states is described by the inverse participation ratio (IPR). Because of the structure disorder, IPR plots for all samples exhibit mobility edges above the valence band maximum (VBM; as defined by the localization to extend transition point). Upon introduction of oxygen-deficient centers, additional defect states appear near the center of the original gap. By looking into the IPR values as well as partial charge density of the defect state (Figure 5d), the electron is found to be spatially localized around the oxygen deficient center. In summary, the removal of the oxygen atom results in the excess



DOI: 10.1021/acsphotonics.8b00769
ACS Photonics 2019, 6, 351−359

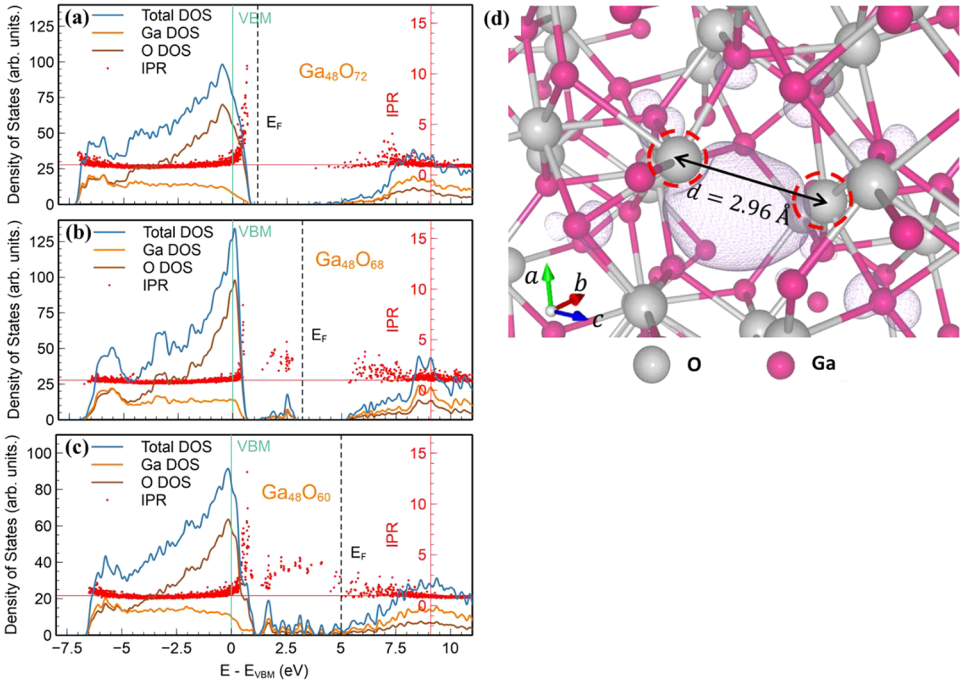


**Figure 5.** Calculated electron structures of neutral and oxygen-deficient *a*-$Ga_2O_3$. (a–c) Total (blue) and atom projected partial DOS of Ga (orange) and O (brown) species. The IPR values of each electron state (red dots) are also included. (d) Partial charge of the highest defect state in the oxygen-deficient ($Ga_{48}O_{68}$) structure. The isosurface is plotted at 0.008 e $Bohr^{-3}$.

Ga sp electrons forming a bounded defect state around the oxygen vacancy, which contributes to an additional localized peak above the original VBM and pushes the Fermi energy upward.

Once the $V_o$ defect is ionized and becomes +2 charged, the neighboring metal atoms will relax away from the vacancy, pushing the $V_o^{2+}$ defect level upward to the bottom of the conduction band.[43] Hence, the upward $V_o^{2+}$ state is a shallow donor, quite different from the neutral deep $V_o$ state. This transformation process has been supposed in *a*-IGZO and *a*-$HfO_2$[43] theoretically. In experimentation, $V_o$ in ZnO is deduced to be +2 charged and responsible for the unintentional n-type doping.[44] Thus, as illustrated in Figure 6a, when

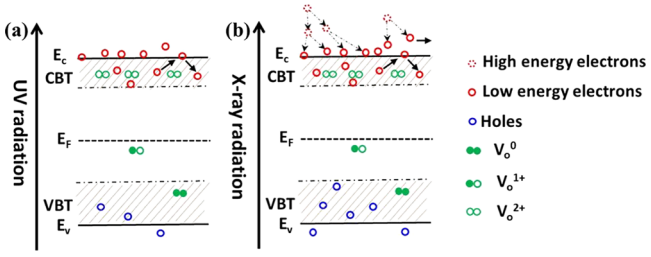


**Figure 6.** Schematic energy band diagrams illustrating the conductive electrons released from valence band, VBT states, and ionization of $V_o$ under (a) UV and (b) X-ray radiation, respectively.

UV light collides onto the samples, except for the generation of e–h pairs from band to band transitions (including band tail states), electrons from neutral deep $V_o$ defects are also released into the conduction band accompanied by the formation of the shallow donor $V_o^{2+}$ states. A dynamic equilibrium between the formation and neutralization of $V_o^{2+}$ states causes a slow saturation of the photocurrent during photo-excitation. As for the dark relaxation, there are two annihilation pathways for the photo-induced carriers: recombination of e–h pairs and neutralization of $V_o^{2+}$ states.[27] It is reported that there is an energy barrier (~0.97 eV) to neutralize the $V_o^{2+}$ states,[45] and thus, we can assume that the second annihilation pathway determines the final dark relaxation time. From the fitting results listed in Table 1, the decay time after UV radiation increases from 0.06 s in D2 to 5.01 s in D5, indicating a slower annihilation rate in samples with smaller oxygen flux, which will in turn improve the quasi-equilibrium photo-induced carrier concentration under illumination. When the illumination source is X-rays, since the energy of X-ray photons (~tens of keV) is significantly higher than that of UV light, the absorption coefficient of X-rays is very small (nearly 1‰ photons can be absorbed by the active layer). Thanks to the high energy of X-rays, high-energy electrons are created as shown in Figure 6b. If these high-energy electrons locate at a few nanometers below the sample surface, they can escape from the material and make a contribution to the air ionization effect.[29] At the same time, because of the electron escape process, a photochemical reaction will happen at the surface, which will change the stoichiometry of the surface with the occurrence of oxygen deficiency.[46] Most of the high-energy electrons exist in the whole active layer because of the good penetrability of X-rays. Such electrons will impact atoms around them and transfer their excessive energy by the creation of new e–h pairs, which is like the cascade effect and can compensate the drawback of low absorption in such a thin film. More importantly, a key factor for the generation of detectable X-ray-induced charge carriers is the small annihilation rate, especially when the absorption rate and the optical band gap are almost identical. In our case, this is achieved by the introduction of $V_o$ states, which will not only slow down the annihilation rate, but also lower the SBHs and enlarge the VBTs. All of these effects are beneficial for the enhancement of the final photocurrent.



DOI: 10.1021/acsphotonics.8b00769
*ACS Photonics* 2019, 6, 351–359

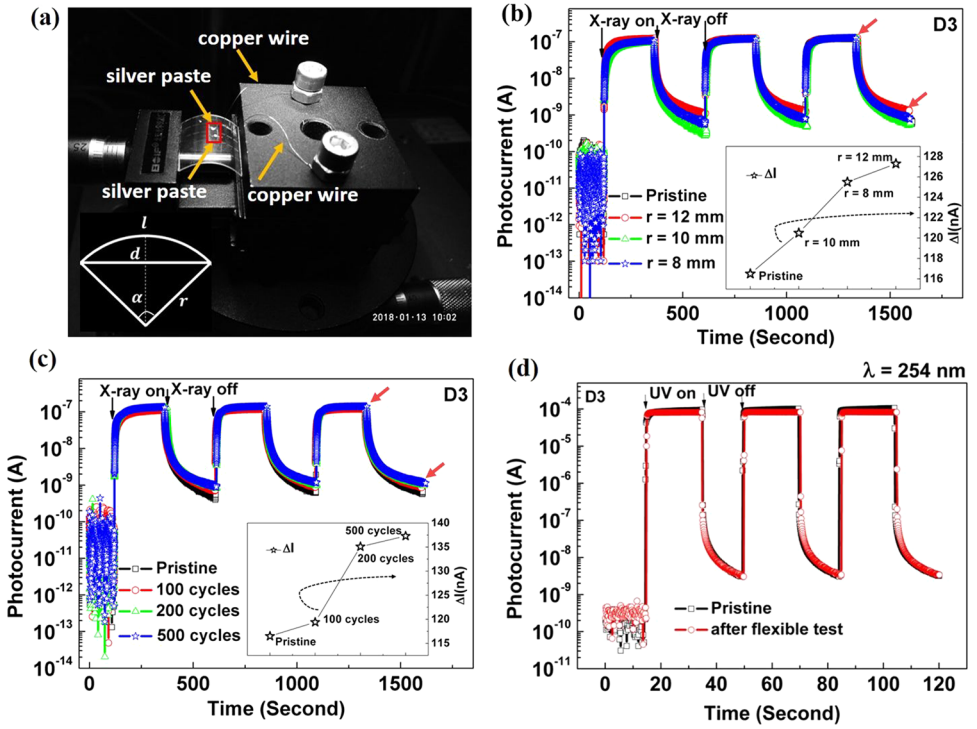


**Figure 7.** (a) *In situ* photograph of the flexible device under a bending test. (b) Time-dependent photoresponse performance of D3 exposed to X-rays under flat and different bending radii. (c) Time-dependent photoresponse of D3 exposed to X-rays at the flat state after bending 0, 100, 200, and 500 cycles with $r$ = 8 mm. (d) Time-dependent photoresponse of D3 exposed to UV 254 nm light after all of the flexibility tests.

Finally, temporal response measurements in different bent states and after hundreds of bending cycles were carried out to evaluate the flexibility of this X-ray detector. Figure 7a is an *in situ* photograph of the flexible device under a bending test. The device was curved by a movable optical bench. On the basis of the geometrical relationship shown in the inset of Figure 7a, we can calculate the bending radius $r$ according to the displacement $d$, which can be read out by the screw micrometer on the left side of the optical bench. Conductive silver paste was used to couple the indium tin oxide (ITO) electrodes of the prototype device (as indicated in the red rectangle) to the connection terminals through thin copper wires. Temporal responses of D3 at different bending radii were first tested as shown in Figure 7b. The device performed almost the same as the pristine one when under different bent states, suggesting that the effect of bending stress on the device performance is ignorable. Figure 7c shows the temporal photoresponse of the same device exposed to X-rays at the flat state after bending 0, 100, 200, and 500 cycles with $r$ = 8 mm. The fatigue tests present almost the same curves even after 500 folding cycles, indicating the robust flexibility of the device. More importantly, from the insets of Figure 7b,c, it can be clearly seen that all $\Delta I$ values ($\Delta I = I_{ph} - I_{dark}$, the $I_{ph}$ and $I_{dark}$ are labeled by the red arrows corresponding to the third cycle of the X-ray on and off in Figure 7b,c) have been increased compared with the pristine ones. The measurement sequence of the device is $r$ = 10, 8, 12 mm, and then the fatigue test after 100, 200, and 500 bending cycles. It seems that the enhancement of the $\Delta I$ value is quite related to the measurement sequence. In addition, from the result of the pulsed X-ray detection using the same device as shown in Figure S3, it can be found that both the photocurrent and dark current increase gradually pulse-by-pulse, which can be attributed to the accumulation of the PPC effect. On the basis of all of the above-mentioned facts, the reason why the $\Delta I$ value is enhanced sequentially during the bending test is tentatively ascribed to the PPC effect. In this case, the degradation level of the device sensitivity after the bending tests cannot be quantitatively calculated or even qualitatively estimated. That is, it is not feasible to recognize the radiation damage in the present stage, which is definitely an interesting topic and needs to be investigated further. On the other hand, we made an evaluation of the UV response of this device after the bending test, which is shown in Figure 7d. It still behaves like a decent UV detector without any obvious degradation, which may result from the amorphous nature of *a*-$Ga_2O_3$ thin film, demonstrating a good robustness of this flexible X-ray detector.

## CONCLUSION

In summary, flexible X-ray detectors based on *a*-$Ga_2O_3$ thin films with finely tuned $V_o$ concentration were successfully explored. Upon a decrease in the oxygen flux during the sputtering process, $V_o$ concentration in the films increased accordingly, which would not only lower the SBHs on the ITO/$Ga_2O_3$ interface, but also generate large density of VBT states. In addition to that, the annihilation rate was impeded because of the neutralization of the ionized oxygen vacancies, resulting in a pronounced PPC effect and remarkable enhancement of the photocurrents induced by X-rays. A much higher S/N ratio (>$10^4$ in D4) was achieved. Additionally, no significant degradation was observed during the bending and fatigue tests. These findings reveal the possibility of *a*-$Ga_2O_3$ in fabrication of flexible X-ray detectors, and also provide a potential way to design novel X-ray detectors using other abundant oxide materials.



DOI: 10.1021/acsphotonics.8b00769
*ACS Photonics* 2019, 6, 351−359

## MATERIALS AND METHODS

**Film Growth.** $Ga_2O_3$ thin films with the thickness of about 250 nm were deposited on PEN (125 $\mu$m thick) substrates by a RF magnetron sputtering system at RT. The $Ga_2O_3$ ceramic target was 5N pure. The PEN substrates were ultrasonically cleaned in acetone, alcohol, and deionized water, successively, and finally blown dry by nitrogen gas. Before deposition, the vacuum was evacuated to the base pressure of $3.0 \times 10^{-4}$ Pa. Then, high-purity oxygen gas was introduced into the sputtering chamber through a leakage valve, the amount of which was monitored by an ion gauge. In the following, the sputtering gas argon (Ar) entered into the chamber through a mass flow controller (MFC) maintained at 10 sccm. *A*-$Ga_2O_3$ thin film was synthesized on PEN substrates for 30 min with a sputtering power of 60 W and a total pressure of 0.4 Pa. Five samples were grown with different oxygen partial pressure: $1.6 \times 10^{-3}$ Pa (D1), $1.4 \times 10^{-3}$ Pa (D2), $1.2 \times 10^{-3}$ Pa (D3), $1.0 \times 10^{-3}$ Pa (D4), and 0 (D5, pure Ar).

**Photodetector Fabrication.** The *a*-$Ga_2O_3$ X-ray detectors were constructed with coplanar interdigital MSM structure by conventional UV-lithography and lift-off technology. The prototype device has 75 pair fingers with 5 $\mu$m in width, 5 $\mu$m in spacing gap, and 300 $\mu$m in length. Indium tin oxide (ITO), 100 nm, was used to form the transparent interdigital electrodes.

**Characterization.** The dark *I*−*V* tests were carried out in air using a source-measurement unit in the Keithley 4200 semiconductor characterization system. Time-dependent response under UV illumination was performed using a hand-held lamp with 254 or 365 nm UV light. The photoresponses of D1, D2, and D5 with various wavelengths were performed with the Omni-$\lambda$ 180i grating spectrometer. The X-ray source was an X-ray tube with a Cu anode, working at 40 kV and 200 mA from an X-ray diffraction setup (Smartlab, Rigaku). A picoammeter (Keithley 6487) was used to record the current variation under both UV light and X-ray irradiation.

**DFT Calculation.** The low-temperature amorphous structures of neutral ($Ga_{48}O_{72}$) and oxygen-deficient $Ga_2O_3$ ($Ga_{48}O_{68}$, $Ga_{48}O_{60}$) are generated by *ab initio* molecular dynamics (AIMD) simulation. In the AIMD simulation, the structure is equilibrated for 3 ps at 10 equally separated temperatures decreasing from 2000 to 500 K. The MD time step is set to 1.5 fs, and the NVT ensemble is used. To account for the volume expansion at high temperature, the volume of the structure is scaled down at the same time from $1.04V_0$ to $1.0V_0$ where $V_0$ is the volume of the initial crystalline structure. The MD-generated structure is fully optimized until all force components are smaller than 0.05 eV $Å^{-1}$. The AIMD simulation uses a kinetic energy cutoff of 280 eV and a single $\Gamma$ point to sample the Brillouin zone while a 400 eV cutoff and $2 \times 2 \times 2$ *K*-point mesh are used for structure optimization.

## ASSOCIATED CONTENT

### Supporting Information

The Supporting Information is available free of charge on the ACS Publications website at DOI: 10.1021/acsphotonics.8b00769.

Partial enlarged detail of time-dependent photocurrents; stretched exponential fitting results; time-dependent photocurrent; and calculation of the dose rate (PDF)

## AUTHOR INFORMATION


### Corresponding Authors

*E-mail: hlliang@iphy.ac.cn.
*E-mail: zxmei@iphy.ac.cn.

### ORCID

Huili Liang: 0000-0002-5164-4290
Pengfei Guan: 0000-0002-7679-6768


### Notes

The authors declare no competing financial interest.

## ACKNOWLEDGMENTS

This work was supported by the National Natural Science Foundation of China (Grants 11675280, 11674405, 61306011, 11274366, 51272280, and 61874139). The authors are grateful for the technical support from the Laboratory of Microfabrication in Institute of Physics, Chinese Academy of Sciences.

## REFERENCES


(1) Marrs, M.; Bawolek, E.; Smith, J. T.; Raupp, G. B.; Morton, D. Flexible Amorphous Silicon PIN Diode X-Ray Detectors. *Proc. SPIE* **2013**, *8730*, 87300C−1.

(2) Gelinck, G. H.; Kumar, A.; Moet, D.; van der Steen, J. L. P. J.; van Breemen, A. J. J. M.; Shanmugam, S.; Langen, A.; Gilot, J.; Groen, P.; Andriessen, R.; Simon, M.; Ruetten, W.; Douglas, A. U.; Raaijmakers, R.; Malinowski, P. E.; Myny, K. X-Ray Detector-on-Plastic With High Sensitivity Using Low Cost, Solution-Processed Organic Photodiodes. *IEEE Trans. Electron Devices* **2016**, *63*, 197−204.

(3) Gelinck, G. H.; Kumar, A.; Moet, D.; van der Steen, J. L.; Shafique, U.; Malinowski, P. E.; Myny, K.; Rand, B. P.; Simon, M.; Rütten, W.; Douglas, A.; Jorritsma, J.; Heremans, P.; Andriessen, R. X-ray imager using solution processed organic transistor arrays and bulk heterojunction photodiodes on thin, flexible plastic substrate. *Org. Electron.* **2013**, *14*, 2602−2609.

(4) Oliveira, J.; Correia, V.; Sowade, E.; Etxebarria, I.; Rodriguez, R. D.; Mitra, K. Y.; Baumann, R. R.; Lanceros-Mendez, S. Indirect X-ray Detectors Based on Inkjet-Printed Photodetectors with a Screen-Printed Scintillator Layer. *ACS Appl. Mater. Interfaces* **2018**, *10*, 12904−12912.

(5) Oliveira, J.; Correia, V.; Costa, P.; Francesko, A.; Rocha, G.; Lanceros-Mendez, S. Stretchable scintillator composites for indirect X-ray detectors. *Composites, Part B* **2018**, *133*, 226−231.

(6) Oliveira, J.; Martins, P. M.; Correia, V.; Hilliou, L.; Petrovykh, D.; Lanceros-Mendez, S. Water based scintillator ink for printed X-ray radiation detectors. *Polym. Test.* **2018**, *69*, 26−31.

(7) Sun, H.; Zhao, B.; Yang, D.; Wangyang, P.; Gao, X.; Zhu, X. Flexible X-ray detector based on sliced lead iodide crystal. *Phys. Status Solidi RRL* **2017**, *11*, 1600397.

(8) Basiricò, L.; Ciavatti, A.; Cramer, T.; Cosseddu, P.; Bonfiglio, A.; Fraboni, B. Direct X-ray photoconversion in flexible organic thin film devices operated below 1 V. *Nat. Commun.* **2016**, *7*, 13063.

(9) Fraboni, B.; Ciavatti, A.; Merlo, F.; Pasquini, L.; Cavallini, A.; Quaranta, A.; Bonfiglio, A.; Fraleoni-Morgera, A. Organic Semiconducting Single Crystals as Next Generation of Low-Cost, Room-Temperature Electrical X-ray Detectors. *Adv. Mater.* **2012**, *24*, 2289−2293.

(10) Yakunin, S.; Sytnyk, M.; Kriegner, D.; Shrestha, S.; Richter, M.; Matt, G. J.; Azimi, H.; Brabec, C. J.; Stangl, J.; Kovalenko, M. V.; Heiss, W. Detection of X-ray photons by solution-processed lead halide perovskites. *Nat. Photonics* **2015**, *9*, 444−450.

(11) Wei, H.; Fang, Y.; Mulligan, P.; Chuirazzi, W.; Fang, H. H.; Wang, C.; Ecker, B. R.; Gao, Y.; Loi, M. A.; Cao, L.; Huang, J. Sensitive X-ray detectors made of methylammonium lead tribromide perovskite single crystals. *Nat. Photonics* **2016**, *10*, 333−340.




DOI: 10.1021/acsphotonics.8b00769
*ACS Photonics* 2019, 6, 351−359

(12) Wei, W.; Zhang, Y.; Xu, Q.; Wei, H.; Fang, Y.; Wang, Q.; Deng, Y.; Li, T.; Gruverman, A.; Cao, L.; Huang, J. Monolithic integration of hybrid perovskite single crystals with heterogenous substrate for highly sensitive X-ray imaging. *Nat. Photonics* **2017**, *11*, 315−322.
(13) Shrestha, S.; Fischer, R.; Matt, G. J.; Feldner, P.; Michel, T.; Osvet, A.; Levchuk, I.; Merle, B.; Golkar, S.; Chen, H.; Tedde, S. F.; Schmidt, O.; Hock, R.; Rührig, M.; Göken, M.; Heiss, W.; Anton, G.; Brabec, C. J. High-performance direct conversion X-ray detectors based on sintered hybrid lead triiodide perovskite wafers. *Nat. Photonics* **2017**, *11*, 436−441.
(14) Wei, H.; DeSantis, D.; Wei, W.; Deng, Y.; Guo, D.; Savenije, T. J.; Cao, L.; Huang, J. Dopant compensation in alloyed $CH_3NH_3PbBr_{3-x}Cl_x$ perovskite single crystals for gamma-ray spectroscopy. *Nat. Mater.* **2017**, *16*, 826−834.
(15) Yakunin, S.; Dirin, D. N.; Shynkarenko, Y.; Morad, V.; Cherniukh, I.; Nazarenko, O.; Kreil, D.; Nauser, T.; Kovalenko, M. V. Detection of gamma photons using solution-grown single crystals of hybrid lead halide perovskites. *Nat. Photonics* **2016**, *10*, 585−591.
(16) Ciavatti, A.; Cramer, T.; Carroli, M.; Basiricò, L.; Fuhrer, R.; De Leeuw, D. M.; Fraboni, B. Dynamics of direct X-ray detection processes in high-Z $Bi_2O_3$ nanoparticles-loaded PFO polymer-based diodes. *Appl. Phys. Lett.* **2017**, *111*, 183301.
(17) Duboz, J. Y.; Beaumont, B.; Reverchon, J. L.; Wieck, A. D. Anomalous photoresponse of GaN x-ray Schottky detectors. *J. Appl. Phys.* **2009**, *105*, 114512.
(18) Liu, L. Y.; Ouyang, X. P.; Zhang, J. F.; Jin, P.; Su, C. L. Properties comparison between nanosecond X-ray detectors of polycrystalline and single-crystal diamond. *Diamond Relat. Mater.* **2017**, *73*, 248−252.
(19) Motoki, K.; Miyazawa, Y.; Kobayashi, D.; Ikegami, M.; Miyasaka, T.; Yamamoto, T.; Hirose, K. Degradation of $CH_3NH_3PbI_3$ perovskite due to soft x-ray irradiation as analyzed by an x-ray photoelectron spectroscopy time-dependent measurement method. *J. Appl. Phys.* **2017**, *121*, No. 085501.
(20) Nomura, K.; Ohta, H.; Takagi, A.; Kamiya, T.; Hirano, M.; Hosono, H. Room-temperature fabrication of transparent flexible thin-film transistors using amorphous oxide semiconductors. *Nature* **2004**, *432*, 488−492.
(21) Zhang, Y. H.; Mei, Z. X.; Cui, S. J.; Liang, H. L.; Liu, Y. P.; Du, X. L. Flexible Transparent Field-Effect Diodes Fabricated at Low-Temperature with All-Oxide Materials. *Adv. Electron. Mater.* **2016**, *2*, 1500486.
(22) Cui, S. J.; Mei, Z. X.; Zhang, Y. H.; Liang, H. L.; Du, X. L. Room-Temperature Fabricated Amorphous $Ga_2O_3$ High-Response-Speed Solar-Blind Photodetector on Rigid and Flexible Substrates. *Adv. Opt. Mater.* **2017**, *5*, 1700454.
(23) Zhao, X.; Chen, L.; He, Y.; Liu, J.; Peng, W.; Huang, Z.; Qi, X.; Pan, Z.; Zhang, W.; Zhang, Z.; Ouyang, X. Nanosecond X-ray detector based on high resistivity ZnO single crystal. *Appl. Phys. Lett.* **2016**, *108*, 171103.
(24) Endo, H.; Chiba, T.; Meguro, K.; Takahashi, K.; Fujisawa, M.; Sugimura, S.; Narita, S.; Kashiwaba, Y.; Sato, E. Fabrication and characterization of a ZnO X-ray sensor using a high-resistivity ZnO single crystal grown by the hydrothermal method. *Nucl. Instrum. Methods Phys. Res., Sect. A* **2011**, *665*, 15−18.
(25) Qian, L. X.; Wu, Z. H.; Zhang, Y. Y.; Lai, P. T.; Liu, X. Z.; Li, Y. R. Ultrahigh-responsivity, rapid-recovery, solar-blind photodetector based on highly nonstoichiometric amorphous gallium oxide. *ACS Photonics* **2017**, *4*, 2203−2211.
(26) Lany, S.; Zunger, A. Anion vacancies as a source of persistent photoconductivity in II-VI and chalcopyrite semiconductors. *Phys. Rev. B: Condens. Matter Mater. Phys.* **2005**, *72*, No. 035215.
(27) Lee, M.; Lee, W.; Choi, S.; Jo, J. W.; Kim, J.; Park, S. K.; Kim, Y. H. Brain-Inspired Photonic Neuromorphic Devices using Photodynamic Amorphous Oxide Semiconductors and their Persistent Photoconductivity. *Adv. Mater.* **2017**, *29*, 1700951.
(28) Cramer, T.; Sacchetti, A.; Lobato, M. T.; Barquinha, P.; Fischer, V.; Benwadih, M.; Bablet, J.; Fortunato, E.; Martins, R.; Fraboni, B. Radiation-Tolerant Flexible Large-Area Electronics Based on Oxide Semiconductors. *Adv. Electron. Mater.* **2016**, *2*, 1500489.
(29) Brivio, D.; Ada, E.; Sajo, E.; Zygmanski, P. Effective contact potential of thin film metal-insulator nanostructures and its role in self-powered nanofilm x-ray sensors. *ACS Appl. Mater. Interfaces* **2017**, *9*, 11258−11265.
(30) Tromson, D.; Bergonzo, P.; Brambilla, A.; Mer, C.; Foulon, F.; Amosov, V. N. Thermally stimulated current investigations on diamond x-ray detectors. *J. Appl. Phys.* **2000**, *87*, 3360−3364.
(31) Jeon, S.; Ahn, S. E.; Song, I.; Kim, C. J.; Chung, U. I.; Lee, E.; Yoo, I.; Nathan, A.; Lee, S.; Ghaffarzadeh, K.; Robertson, J.; Kim, K. Gated three-terminal device architecture to eliminate persistent photoconductivity in oxide semiconductor photosensor arrays. *Nat. Mater.* **2012**, *11*, 301−305.
(32) Masuzawa, T.; Kuniyoshi, S.; Onishi, M.; Kato, R.; Saito, I.; Yamada, T.; Koh, A. T. T.; Chua, D. H. C.; Shimosawa, T.; Okano, K. Conditions for a carrier multiplication in amorphous-selenium based photodetector. *Appl. Phys. Lett.* **2013**, *102*, No. 073506.
(33) Kasap, S. O. X-ray sensitivity of photoconductors: application to stabilized a-Se. *J. Phys. D: Appl. Phys.* **2000**, *33*, 2853−2865.
(34) Bube, R. H.; Echeverria, L.; Redfield, D. Evidence for a stretched-exponential description of optical defect generation in hydrogenated amorphous silicon. *Appl. Phys. Lett.* **1990**, *57*, 79−80.
(35) Luo, J.; Adler, A. U.; Mason, T. O.; Bruce Buchholz, D.; Chang, R. P. H.; Grayson, M. Transient photoresponse in amorphous In-Ga-Zn-O thin films under stretched exponential analysis. *J. Appl. Phys.* **2013**, *113*, 153709.
(36) Kang, Y.; Song, H.; Nahm, H. H.; Jeon, S. H.; Cho, Y.; Han, S. Intrinsic nature of visible-light absorption in amorphous semiconducting oxides. *APL Mater.* **2014**, *2*, No. 032108.
(37) Davis, E. A.; Mott, N. F. Conduction in non-crystalline systems V. Conductivity, optical absorption and photoconductivity in amorphous semiconductors. *Philos. Mag.* **1970**, *22*, 0903−0922.
(38) Jang, J. T.; Park, J.; Ahn, B. D.; Kim, D. M.; Choi, S. J.; Kim, H. S.; Kim, D. H. Study on the Photoresponse of Amorphous In−Ga−Zn−O and Zinc Oxynitride Semiconductor Devices by the Extraction of Sub-Gap-State Distribution and Device Simulation. *ACS Appl. Mater. Interfaces* **2015**, *7*, 15570−15577.
(39) Ryu, B.; Noh, H. K.; Choi, E. A.; Chang, K. J. O-vacancy as the origin of negative bias illumination stress instability in amorphous In−Ga−Zn−O thin film transistors. *Appl. Phys. Lett.* **2010**, *97*, No. 022108.
(40) Kresse, G.; Joubert, D. From ultrasoft pseudopotentials to the projector augmented-wave method. *Phys. Rev. B: Condens. Matter Mater. Phys.* **1999**, *59*, 1758−1775.
(41) Perdew, J. P.; Burke, K.; Ernzerhof, M. Generalized Gradient Approximation Made Simple. *Phys. Rev. Lett.* **1996**, *77*, 3865−3868.
(42) Heyd, J.; Scuseria, G. E.; Ernzerhof, M. Erratum: "Hybrid functionals based on a screened Coulomb potential" [J. Chem. Phys. 118, 8207 (2003)]. *J. Chem. Phys.* **2006**, *124*, 219906.
(43) Robertson, J. Mott lecture: How bonding concepts can help understand amorphous semiconductor behavior. *Phys. Status Solidi A* **2016**, *213*, 1641−1652.
(44) Liu, L. S.; Mei, Z. X.; Tang, A. H.; Azarov, A.; Kuznetsov, A.; Xue, Q. K.; Du, X. L. Oxygen vacancies: The origin of n-type conductivity in ZnO. *Phys. Rev. B: Condens. Matter Mater. Phys.* **2016**, *93*, 235305.
(45) Nahm, H. H.; Kim, Y. S.; Kim, D. H. Instability of amorphous oxide semiconductors via carrier-mediated structural transition between disorder and peroxide state. *Phys. Status Solidi B* **2012**, *249*, 1277−1281.
(46) Kohiki, S.; Hatta, S.; Setsune, K.; Wasa, K.; Sakai, M.; Fukushima, S.; Gohshi, Y. X-ray irradiation effects on superconductivity of cuprate superconductor thin films. *J. Appl. Phys.* **1991**, *70*, 6945−6951.


DOI: 10.1021/acsphotonics.8b00769
*ACS Photonics* 2019, 6, 351−359